Solid State Sciences 25 (2013) 55–62

Contents lists available at ScienceDirect

Solid State Sciences

journal homepage: www.elsevier.com/locate/ssscie

Changes in electronic, magnetic and bonding properties from Zr_2FeH_5 to Zr_3FeH_7 addressed from ab initio

S.F. Matar [a,b,*], A.F. Al Alam [c,d], D. Gédéon [e], N. Ouaini [c]

[a] CNRS, ICMCB, UPR 9048, F-33600 Pessac, France
[b] Univ. Bordeaux, ICMCB, UPR 9048, F-33600 Pessac, France
[c] Université Saint-Esprit de Kaslik (USEK), Groupe OCM (Optimisation et Caractérisation des Matériaux), CSR-USEK, CNRS-L, Jounieh, Lebanon
[d] American University of Science and Technology (AUST), Department of Mathematics, Beirut, Lebanon
[e] Lebanese Ministry of Industry, Beirut, Lebanon

ARTICLE INFO

Article history:
Received 7 June 2013
Received in revised form
2 August 2013
Accepted 5 August 2013
Available online 17 August 2013

Keywords:
DFT
Bonding
Bulk modulus
Electronic structure
Hydrides

ABSTRACT

Potential hydrogen storage ternaries Zr_3FeH_7 and Zr_2FeH_5, are studied from ab initio with the purpose of identifying changes in electronic structures and bonding properties. Cohesive energy trends: $E_{coh.}(ZrH_2) > E_{coh.}(Zr_2FeH_5) > E_{coh.}(Zr_3FeH_7) > E_{coh.}$ (hypothetic-FeH) indicate a progressive destabilization of the binary hydride ZrH_2 through adjoined Fe so that Zr_3FeH_7 is found less cohesive than Zr_2FeH_5. From the energy volume equations of states EOS the volume increase upon hydriding the intermetallics leads to higher bulk moduli B_0 explained by the Zr/Fe–H bonding. Fe–H bond in Zr_2FeH_5 leads to annihilate magnetic polarization on Fe whereas Fe magnetic moment develops in Zr_3FeH_7 identified as ferromagnetic in the ground state. These differences in magnetic behaviors are due to the weakly ferromagnetic Fe largely affected by lattice environment, as opposed to strongly ferromagnetic Co. Hydrogenation of the binary intermetallics weakens the inter-metal bonding and favors the metal–hydrogen bonds leading to more cohesive hydrides as with respect to the pristine binaries. Charge analyses point to covalent like Fe versus ionic Zr and hydrogen charges ranging from covalent $H^{-0.27}$ to more ionic $H^{-0.5}$.

1. Introduction

Intermetallics are strong candidates for hydrogen storage/release from a double-folded interest: (i) their capacity of uptaking relatively large H amounts, and (ii) their potentiality in on-board vehicular, portable, stationary, bulk, fuel cell batteries and transport applications. The latter feature solved the difficulty encountered with archetype metal hydride MgH_2 characterized by a high gravimetric density (7.6 wt. % H_2). Nevertheless, its strong Mg–H bonding and subsequent high desorption temperature (~350 °C) prevent its *ad hoc* use for applications [1]. However it was recently shown that carbon modified MgH_2 either at the surface or by insertion had better desorption capacities as investigated both experimentally [2,3] and theoretically [4].

Efforts to reduce the desorption temperature involved intensive experimental and theoretical research such as the study of adjoined transition metals T leading to ternary Mg–T–H hydrides (e.g. Mg_2NiH_4 [5,6]) with a covalent character of H brought by T. Among the ternaries, hydrido-complexes such as Mg_2CoH_5 [7] are synthesized from mixtures of Mg and Co because Mg_2Co intermetallic does not exist. This is opposed to Zr–T based hydrides. Zr_3FeH_7 and Zr_2FeH_5 are obtained by the hydrogenation of the corresponding zirconium binaries: Zr_3Fe and Zr_2Fe [8,9]. They are the only Zr-rich intermetallics in the Zr–Fe phase diagram [10], i.e. with no mention of equiatomic ZrFe intermetallic. It is important to note that the cubic C15 Laves phase $ZrFe_2$ also absorbs large amounts of hydrogen [11].

Zr_3Fe [12] belongs to the Re_3B aristotype structure with base centered orthorhombic (*Cmcm* space group). The structure and symmetry (see Table 1) are retained upon hydrogenation (deuteration for neutron diffraction experiments) [8]. The resulting positions for hydrogen were determined in the following interstices: trigonal bipyramidal [Zr_3Fe_2] and tetrahedral [Zr_3Fe] and [Zr_4]. Hydrogenation of Zr_2Fe with five H uptake (Zr_2FeH_5) [9] preserves the tetragonal structure but a change of the centering from *I* to *P* is found, i.e. from body centered *I*4/*mcm* to primitive *P*4/*ncc* space group. This change is due to the occupation of one of the two

* Corresponding author. CNRS, ICMCB, UPR 9048, F-33600 Pessac, France.
E-mail addresses: matar@icmcb-bordeaux.cnrs.fr, abouliess@gmail.com (S.F. Matar).

1293-2558/$ – see front matter © 2013 Elsevier Masson SAS. All rights reserved.
http://dx.doi.org/10.1016/j.solidstatesciences.2013.08.002

Table 1
Experimental [8,12] and (calculated) lattice parameters of Zr_3Fe and Zr_3FeH_7.

Cmcm	Zr_3Fe
a/Å	3.321 (3.29)
b	10.966 (10.86)
c	8.825 (8.93)
V/Å^3	321.389 (319.06)
Zr1 (4*c*)	0 9/22(0.420) ¼
Zr2 (8*f*)	0 3/22(0.138) (0.061)
Fe (4*c*)	0 0.73(0.762) ¼
Cmcm	Zr_3FeH_7
a/Å	3.577 (3.505)
b	11.021 (10.95)
c	9.612 (9.73)
V/Å^3	378.96 (373.43)
Zr1 (4*c*)	0 0.421 (0.42) ¼
Zr2 (8*f*)	0 0.139 (0.14) 0.049 (0.04)
Fe (4*c*)	0 0.716 (0.71) ¼
H1 (4*c*)	0 0.222 (0.22) ¼
H2 (8*f*)	0 0.410 (0.41) 0.645 (0.59)
H3 (8*f*)	0 0.328 (0.33) 0.056 (0.06)
H4 (8*f*)	0 0.963 (0.96) 0.129 (0.13)
Dist./Å	
Fe–H1	1.79 (1.75)
Fe–H2	1.71 (1.65)
Zr–H3	2.08 (2.03)
Zr2–H4	2.10 (2.04)

Table 2
Experimental ($T = 4.2$ K) [9] and (calculated) lattice parameters of Zr_2Fe and Zr_2FeH_5.

*I*4/*mcm*	Zr_2Fe
a/Å	6.385 (6.25)
c	5.596 (5.71)
V/Å^3	228.139 (223.05)
Zr (8*f*)	0.162(0.141) 0.675(0.679) 0
Fe (4*c*)	0 0 ¼
*P*4/*ncc*	Zr_2FeH_5
a/Å	6.921 (6.866)
c	5.620 (5.619)
V/Å^3	269.23 (264.89)
Zr (8*f*)	0.411 (0.41) 0.589 (0.59) ¼
Fe (4*c*)	¼ ¼ 0.010 (0.01)
H1 (4*b*)	$^3/_4$ ¼ 0
H2 (16*g*)	0.032 (0.03) 0.165(0.17) 0.076(0.07)
Dist./Å	
Fe–H2	1.66 (1.61)
Zr–H1	2.11 (2.10)
Zr–H2	2.06 (2.05)

crystallographically distinct H sub-lattices of half the 32 [Zr_3Fe] tetrahedral holes in an ordered manner. The second hydrogen (H1) is found in tetrahedral [Zr_4] surrounding.

The shortest interatomic distances in both hydride structures are for Fe–H with *d*(Fe–H) ~1.71 Å in Zr_3FeH_7 and *d*(Fe–H) ~1.66 Å in Zr_2FeH_5. From these observations, peculiarities in the bonding (mainly for Zr–H and Fe–H) may be expected due to the different chemical natures of Zr with $\chi_{Zr} = 1.33$ (Pauling electronegativity), compared to the more electronegative Fe ($\chi_{Fe} = 1.88$) forming the surroundings of H. The small Fe–H distance in the 2:1:5 compound arises *inter alia* from the $[FeH_2]_4$ pyramidal motifs. This is similar to the surrounding of Co by H in the hydrido-complex Mg_2CoH_5 [7]. The different atomic environment of Fe and the larger Fe–H separation in the 3:1:7 compound are likely to drive modifications of the magnetic properties as the onset of magnetization on Fe, oppositely to Zr_2FeH_5 which remains nonmagnetic (as shown hereafter). Such magnetovolume versus chemical bonding effect for the Fe sub-lattice is interesting to identify in these compounds in as far as no iron hydrides are known in the Fe–H phase diagram [13], oppositely to cobalt hydrides and sub-hydrides [14].

These features could be rationalized using appropriate computational tools of energy, charge density and geometry optimization criteria as well as chemical bonding properties indicators within the well-established quantum mechanical framework of the density functional theory (DFT) [15,16]. It is the aim of present work to address such properties for the two binary intermetallics and their hydrogenated homologues comparatively.

2. Computation methods

Two DFT computational methods were used in a complementary manner. The Vienna ab initio simulation package (VASP) code [17,18] allows geometry optimization and energy calculations. This is achieved using the projector augmented wave (PAW) method [18,19], built within the generalized gradient approximation (GGA) scheme following Perdew, Burke and Ernzerhof (PBE) [20]. Also preliminary calculations with local density approximation LDA [21] led to underestimated volumes versus the experiment. The potentials account for the valence state of each atomic component, i.e. no improvement upon including semi-core states could be identified. The conjugate-gradient algorithm [22] is used in this computational scheme to relax the atoms. The tetrahedron method with Blöchl corrections [19] as well as a Methfessel–Paxton [23] scheme, was applied for both geometry relaxation and total energy calculations. Brillouin-zone (BZ) integrals were approximated using the special *k*-point sampling. The optimization of the structural parameters was performed until the forces on the atoms were less than 0.02 eV/Å and all stress components less than 0.003 eV/Å^3. The calculations are converged at an energy cut-off of 400 eV for the plane-wave basis set with respect to the *k*-point integration with $10 \times 10 \times 3$ for Zr_3FeH_7 and $6 \times 6 \times 8$ for Zr_2FeH_5 for best convergence and relaxation to zero strains. The calculations are scalar relativistic.

Then all-electron calculations with GGA were carried out for a full description of the electronic structure and the properties of chemical bonding, using the full potential scalar-relativistic academic code *augmented spherical wave* (ASW) method [24,25]. In the minimal ASW basis set, we chose the outermost shells to represent the valence states and the matrix elements were constructed using partial waves up to $l_{max} + 1 = 3$ for Zr and Fe and $l_{max} + 1 = 1$ for H. Self-consistency was achieved when charge transfers and energy changes between two successive cycles were below 10^{-8} and 10^{-6} eV respectively. BZ integrations were performed using the linear tetrahedron method within the irreducible wedge. In order to optimize the basis set, additional augmented spherical waves are placed at carefully selected interstitial sites (IS). Besides the site projected density of states, we discuss qualitatively the pair interactions based on the overlap population analysis with the crystal orbital overlap population (COOP) [26]. In the plots, positive, negative, and zero COOP indicate bonding, anti-bonding, and non-bonding interactions, respectively.

3. Cohesive energies, equilibrium properties and charges

3.1. Geometry optimization and cohesive energies

For the intermetallics and hydrogenated homologues, the experimental and calculated structure parameters are given in Tables 1 and 2. The calculated values show some differences with respect to experiment especially for H coordinates obtained for the

deuterides in both compounds [8,9]. The calculated shortest distances are smaller but in fair agreement with experimental values which will be used for the discussions in following sections. The agreement is such that it can allow establishing trends between the two compounds as for the energies, the mechanical properties as well as for the relative charge transfers.

The cohesive energies are obtained from the differences between the total energy of the compound and those of the atomic constituents Zr and Fe as well as dihydrogen. The latter three have the following energies from PAW–GGA calculations:

Fe: −7.810 eV/atom, Zr: −8.477 eV/atom and dihydrogen: −6.557 eV/H_2. The total electronic energies for the binary and ternary compounds are:

$E_{TOT.}$ (Zr_3FeH_7) = −123.241 eV (2 FU); $E_{TOT.}$ (Zr_2FeH_5) = −181.314 eV (4 FU).

$E_{TOT.}$ (Zr_3Fe) = −68.542 eV (2 FU); $E_{TOT.}$ (Zr_2Fe) = −51.417 eV (2 FU).

Also we derive the energies for the binary hydrides:

$E_{TOT.}$ (ZrH_2) = −16.82 eV/FU in the fluorite structure and $E_{TOT.}$ (hypothetic-FeH) = −11.483 eV/FU in the rocksalt structure as CoH [13]. The resulting cohesive energies are then: $E_{coh.}$ (ZrH_2) = −0.595 eV/at. and $E_{coh.}$ (FeH) = −0.197 eV/at.

The resulting atom averaged cohesive energies are:

$E_{coh.}$ (Zr_3Fe) = −0.258 eV; $E_{coh.}$ (Zr_3FeH_7) = −0.493 eV; $E_{coh.}$ (Zr_2Fe) = −0.315 eV; $E_{coh.}$ (Zr_2FeH_5) = −0.521 eV.

For the examined hydrides, the trends in atom averaged cohesive energies are:

$E_{coh.}$ (ZrH_2) > $E_{coh.}$ ($ZrFeH_{2.5}$) > $E_{coh.}$ ($ZrFe_{0.33}H_{2.33}$) > $E_{coh.}$ (FeH) i.e. (−0.595 to −0.521 to −0.493 to −0.197).

The results show that the most cohesive compound is ZrH_2 and the least cohesive one is FeH, in agreement with the facts that the hydrides decompose mainly into ZrH_2 upon heating [8,9] on one hand and that 'FeH' is hypothetic on the other hand.

Larger cohesive energies characterize the hydrogenated compounds as with respect to pristine intermetallics. This could arise from different bonding interactions within the structure between the metal constituents on one hand and between hydrogen and the metal substructures on the other hand. Also the trend $E_{coh.}$ (Zr_2Fe) > $E_{coh.}$ (Zr_3Fe) is kept for the hydrogenated compounds and Zr_2FeH_5 is found more cohesive than Zr_3FeH_7. Further assessment of these results should be obtained from the analysis of the chemical bonding discussed in next section.

3.2. Energy–volume equations of state (EOS)

Equilibrium zero pressure parameters can be obtained from the energy–volume (E, V) equation of state (EOS) with (E, V) set of calculations around minima found from geometry optimization. The underlying physics of this procedure is that the calculated total energy corresponds to the cohesion within the crystal in as far as the solution of the Kohn–Sham DFT equations gives the energy with respect to infinitely separated electrons and nuclei. But the zero of energy depends on the choice of the potentials, then energy becomes arbitrary through shifting, not scaling. However the energy derivatives as well as the EOS remain unaltered. For this reason one needs to establish the EOS from which the fit parameters can be extracted for an assessment of the equilibrium values. The calculated data curves (for two formula units) are depicted in Fig. 1 for pristine intermetallics Zr_3Fe and Zr_2Fe and also for their hydrides Zr_3FeH_7 and Zr_2FeH_5. The quadratic variation of the $E(V)$ curves allows their fit with an energy-volume Birch EOS, shown below for a development up to the 3rd order [27]:

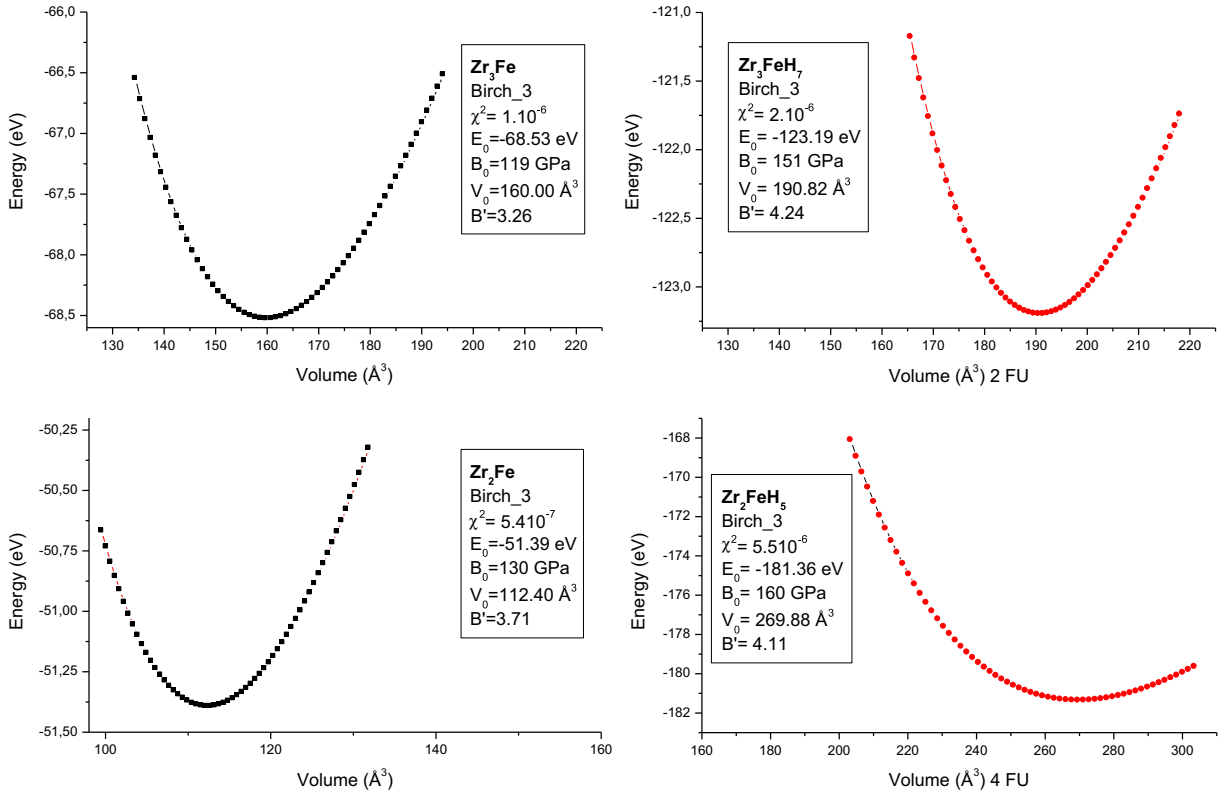

Fig. 1. Energy–volume equations of states of intermetallics Zr_3Fe and Zr_2Fe and of hydrides Zr_3FeH_7 and Zr_2FeH_5.

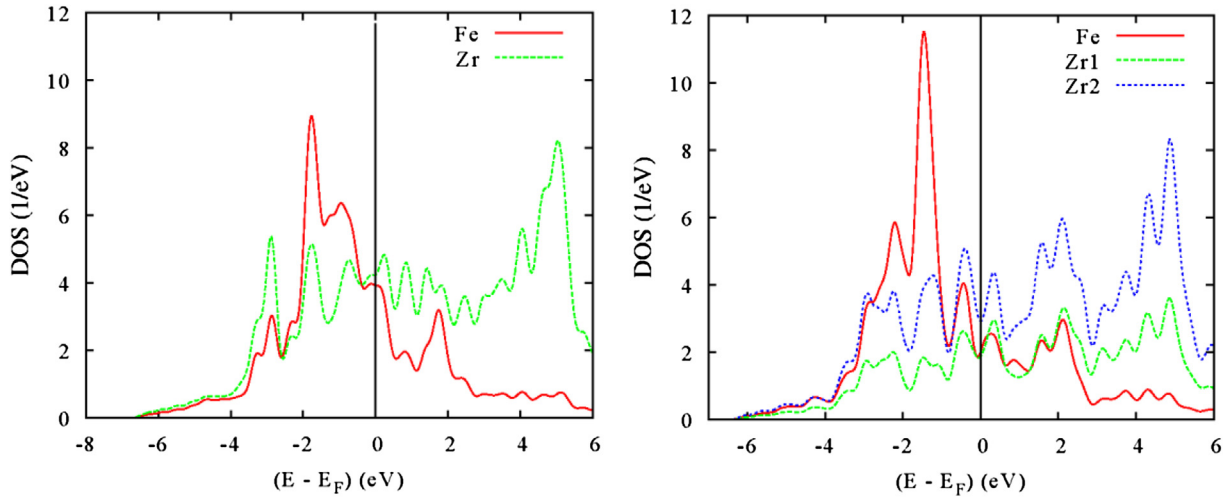

Fig. 2. Site projected density of states of Zr_2Fe (left) and Zr_3Fe (right).

$$E(V) = E_0(V_0) + \frac{9}{8}V_0B_0\left[(V_0/V)^{2/3} - 1\right]^2 + \frac{9}{16}B_0(B' - 4)V_0\left[(V_0/V)^{2/3} - 1\right]^3$$

where E_0, V_0, B_0 and B' are the equilibrium energy, the volume, the bulk modulus and its pressure derivative, respectively.

With small differences, the equilibrium volumes are in agreement with both optimized values and with experiment (Tables 1 and 2). For the intermetallics, the corresponding zero pressure bulk moduli: B_0 (Zr_3Fe) = 119 GPa and B_0 (Zr_2Fe) = 130 GPa follow the volume trends, i.e. the larger the volume the smaller is the bulk modulus. This trend is also found for the hydrogenated compounds: B_0 (Zr_3FeH_7) = 151 GPa and B_0 (Zr_2FeH_5) = 160 GPa but the difference with respect to the intermetallics is higher for Zr_2FeH_5 ($\Delta B_0 = \sim 30$ GPa) as with respect to Zr_3FeH_7 ($\Delta B_0 = \sim 20$ GPa). This can be interpreted as follows: the volume increase upon hydriding should lead to significant lowering of the incompressibility but the bonding of H with the metallic constituents, larger in Zr_2FeH_5 versus Zr_3FeH_7, opposes to this effect. Also the overall magnitudes of the bulk modules ~160 GPa are significant of alloy compounds in as far as they are of smaller magnitudes than in oxides which are in the range of 200–250 GPa and B' values are within range of usually encountered magnitudes [28].

3.3. Charge analysis

We further assess these results by analyzing the charge density issued from the self consistent calculations using the AIM (atoms in molecules theory) approach [29] developed by Bader who devised an intuitive way of splitting molecules into atoms as based purely on the electronic charge density. Typically in chemical systems, the charge density reaches a minimum between atoms and this is a natural region to separate them from each other. Such an analysis can be useful when trends between similar compounds are examined; they do not constitute a tool for evaluating absolute ionizations. Bader's analysis is done using a fast algorithm operating on a charge density grid [30]. The results of computed charges (Q) are such that they lead to neutrality when the respective multiplicities are accounted for (in e unit). The obtained values are:

Zr_3Fe: Q(Zr1) = +0.295(×2); Q(Zr2) = +0.320(×4);
Q(Fe) = −0.935(×2);

Zr_3FeH_7: Q(Zr1) = +1.020(×2); Q(Zr2) = +1.030(×4);
Q(Fe) = −0.313(×2); Q(H1) = −0.275 (×2); Q(H2) = −0.315(×4);
Q(H3) = −0.488(×4); Q(H4) = −0.440(×4);

Zr_2Fe: Q(Zr) = +0.424(×4); Q(Fe) = −0.842(×2);

Zr_2FeH_5: Q(Zr) = +1.024; Q(Fe) = −0.283; Q(H1) = −0.433 (×4);
Q(H2) = −0.333(×16).

In Zr_3Fe due to the large electronegativity difference between Zr and Fe: χ(Zr) = 1.33 versus χ(Fe) = 1.88, charge transfer is observed from Zr towards Fe in a larger magnitude than in Zr_2Fe, i.e. Q(Fe_Zr_3Fe) = −0.925 is lowered to Q(Fe_Zr_2Fe) = −0.842.

When H is introduced, it collects electrons from both Zr and Fe through its coordination within the polyhedra described in the introduction with resulting different magnitudes.

Zr_3FeH_7: covalent like $H1^{-0.275}$ in [Zr_3Fe_2] to less covalent $H3^{-0.488}$ in [Zr_4].

Zr_2FeH_5: covalent like $H2^{-0.333}$ in [Zr_3Fe] to less covalent $H1^{-0.433}$ in [Zr_4].

It can be noted that the larger charge transfer for H2 in Zr_2FeH_5 versus H1 in Zr_3FeH_7 is due to the larger Fe content in the coordination polyhedron.

4. Electronic density of states and chemical bonding properties

In as far as fairly good agreements between experimental and calculated crystal parameters were found (Tables 1 and 2), the electronic density of states and the chemical bonding were analyzed for the two compounds based on experimental data and assuming firstly spin degenerate total spin (NSP) configuration. At self consistent convergence the charge transfer follows the trends observed above with additional charge residues of ~0.15 electrons from the atomic spheres to IS.

4.1. Nonmagnetic and spin polarized calculations

The site projected density of states (PDOS) for Zr_2Fe and Zr_3Fe are shown in Fig. 2. Due to their respective space group I and C centering, the calculations account explicitly for two formula units FU. The abscissa show the energy brought to the Fermi level E_F. The metallic character is exhibited in both panels from the finite DOS at

E_F. Their intensities are larger in the 2:1 versus the 3:1 intermetallic due to the larger Zr content. From their filling at the atomic state Fe (more than half filled 3*d*: $4s^2\ 3d^6$) and Zr (less than half filled 4*d*: $5s^2\ 4d^2$), their PDOS are centered below and above E_F respectively as signaled by the intense peaks. Different PDOS shapes are observed between the two binaries from the sharper PDOS lines in Zr_3Fe as with respect to Zr_2Fe. This signals a less covalent character and illustrates the larger charge transfer obtained above.

Fig. 3 shows the PDOS for Zr_2FeH_5 (2:1:5) and Zr_3FeH_7 (3:1:7). Due to their respective *P* and *C* centerings the DOS are twice larger for the former (4 FU explicitly) as with respect to the latter (2 FU explicitly). With respect to Fig. 3 of the intermetallics, the valence band (VB) located below E_F is significantly modified by the occurrence of extra states due to H presence particularly between −10 and −4 eV and the similar PDOS shapes signal chemical bonding between H and Zr/Fe.

E_F crosses equal Zr and Fe PDOS in the 2:1:5 system as with respect to the 3:1:7 one which exhibits twice larger Fe (PDOS) magnitude. The consequence is the instability of the 3:1:7 compound in such spin degenerate configuration. This is discussed within the Stoner mean field theory of band ferromagnetism [31]. The total energy of the spin system arises from the exchange and kinetic energies. Referring the total energy to the nonmagnetic state (NSP), this is expressed as:

$$E = \frac{1}{2}\left[\frac{m^2}{n(E_F)}\right][1 - In(E_F)]$$

In this expression, *I* is the Stoner integral derived from spin polarized computations and $n(E_F)$ is the PDOS value for a given state −*d*− at E_F in the nonmagnetic state. The unit-less Stoner product $In(E_F)$ provides a stability criterion, i.e. energy is lowered and the spin system stabilizes in a (ferro)magnetically ordered configuration (implicitly) when $In(E_F) > 1$. From quantum theoretical calculations by Janak [32] a value of $I\{Fe(3d)\} = 0.46$ eV was derived. With $n_{Fe}(E_F) = 2.17\ eV^{-1}$, $In(E_F)$ equals 0.99 in 3:1:7 and $n_{Fe}(E_F) = 1.07\ eV^{-1}$, $In(E_F) = 0.49$ in 2:1:5. The close to unity of the Stoner product indicates that Fe is near magnetic instability and could carry a magnetic moment upon spin polarized calculations, oppositely to the 2:1:5 compound where the Stoner product is much lower than 1. In both compounds $n_{Zr}(E_F)$ are too low to obey the Stoner criterion and no spontaneous magnetic polarization could be expected on Zr sites.

Subsequent spin polarized ferromagnetic (SPF) calculations actually lead to a lowering of the total energy by ΔE (SPF–NSP) = −0.1 eV/cell in 3:1:7 and to the onset of a moment $M_{Fe} = 0.38\ \mu_B$ whereas Zr sites carry small magnitude moments of $M_{Zr1} = 0.005\ \mu_B$ and $M_{Zr2} = 0.012\ \mu_B$ arising from the overlapping between the valence states of Zr and Fe. The absence of spin

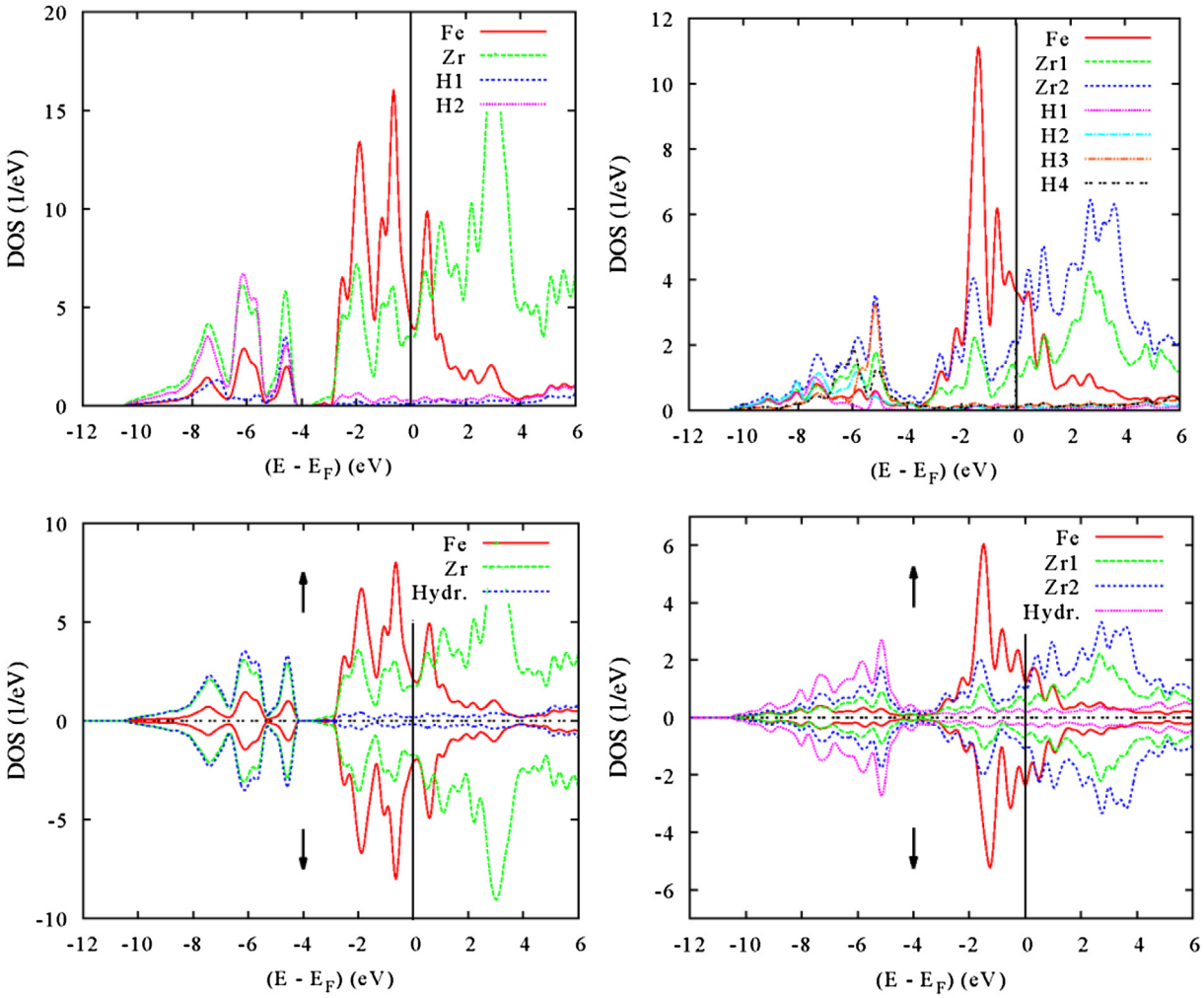

Fig. 3. Site projected density of states of Zr_2FeH_5 (left) and Zr_3FeH_7 (right) in nonmagnetic (NSP) configuration (top) and spin polarized (SP) configuration (bottom).

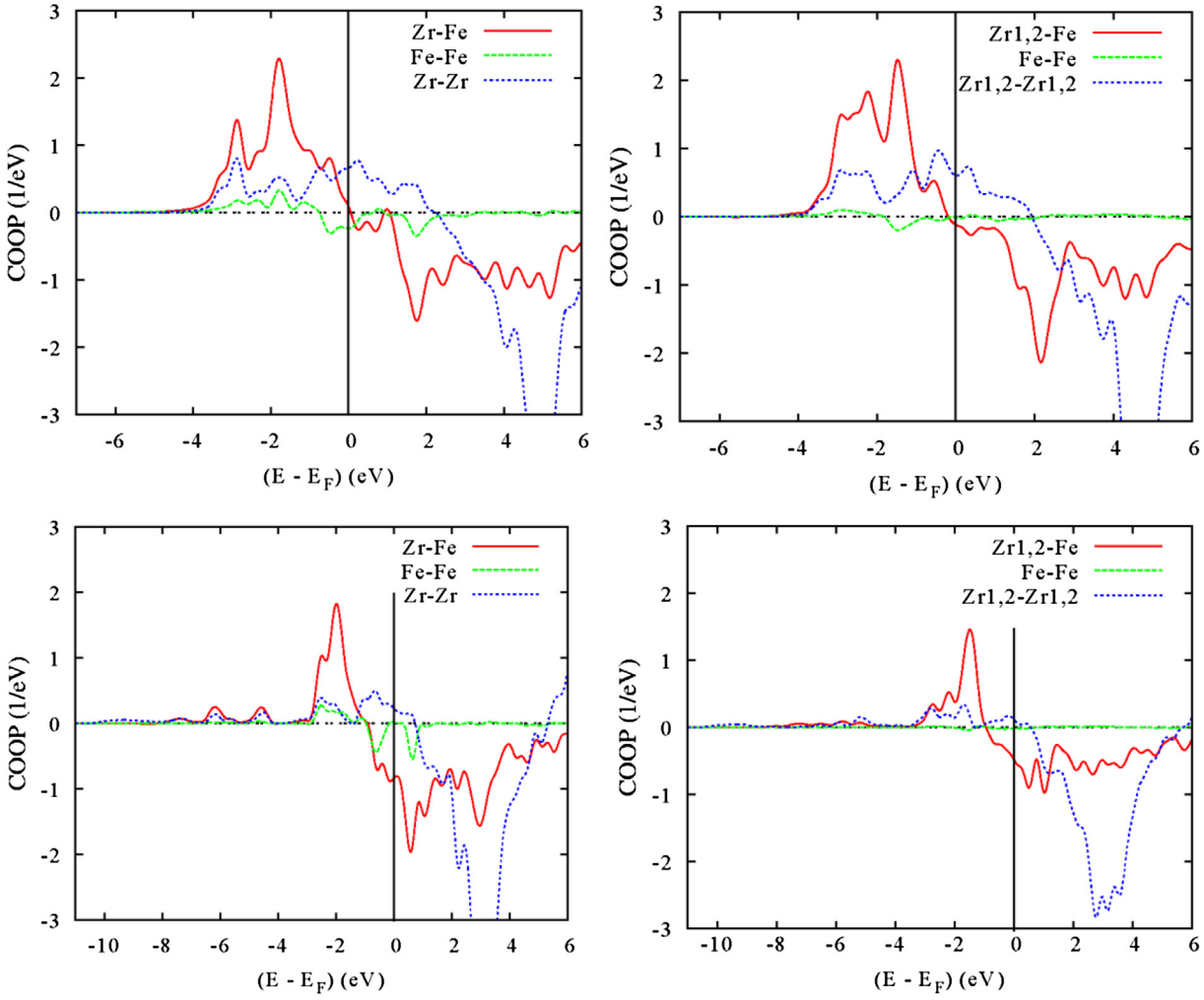

Fig. 4. Bonding within the metal substructures in Zr_2Fe and Zr_3Fe intermetallics (top panels) and corresponding hydrides (bottom).

polarization could be observed for the 2:1:5 compound, in agreement with the Stoner analysis. This is opposite to the calculated moment on Co close to 0.62 μ_B in isostructural Zr_2CoH_5 [33]. Clearly the difference between the two 2:1:5 compounds arise from the nature of the transition metal. Also iron is more affected by the neighborhood of H leading to a vanished magnetization. It is important to mention that the Fe–H separation is smaller in the 2:1:5 compound as with respect to the 3:1:7 hydride. Such high sensitivity to small lattice changes is a signature of the weak ferromagnetic behavior of Fe, i.e. oppositely to strong ferromagnetic Co (and Ni) [31]. Thus it can be argued that Co keeps a significant magnitude of magnetic polarization in Zr_2CoH_5 in spite of its presence in the environment of H whereas such environment destroys the iron magnetism in Zr_2FeH_5 homologue. Finally owing to the Fe–H bonding the magnetic moment on Fe is largely lowered in Zr_3FeH_7, as compared with M(Fe) = 2.12 μ_B in α-Fe. Then, schematically, Fe–H spacing and bonding "tune" the magnetic moment. To the best of our knowledge the magnetic properties of the two ternary hydrides are not known experimentally.

These results are illustrated in the lower panels of Fig. 3 for the site and spin projected PDOS. Their discussion for the respective sites follows from the non magnetic spin degenerate calculations. Further, the magnetic moments arise from a closely rigid energy band shift between majority ↑ spin populations and minority spin ↓ ones. These ↑ and ↓ DOS mirror each other in the 2:1:5 compound, leading to zero exchange splitting and resulting zero magnetic moments whereas there is a small energy shift between these spin DOS in 3:1:7 resulting in a small moment on Fe.

Finally, in order to confirm that the actual magnetic ground state is ferromagnetic, antiferromagnetic SPAF configuration was tested with dispatching the 3:1:7 crystal structure into two magnetic half-subcells, one of them for UP SPINS and the other for DOWN SPINS. The result is zero magnetization as expected from full compensation between the two magnetic sub-cells, and a raise of the energy by ΔE (SPAF–SPF) = +0.12 eV/cell. Thus the magnetic ground state is predicted to be ferromagnetic.

4.2. Bonding properties

Figs. 4 and 5 show the chemical bonding discussed using the COOP criterion. Considering firstly the change of inter-metal bonding in the intermetallics versus the hydrogenated compounds, Fig. 4 presents the plots in four panels considering one atom of each kind for the sake of establishing comparisons. The metal–metal bonding is predominantly of hetero atomic nature, i.e. Zr–Fe bonding is dominating over Zr–Zr and Fe–Fe which is found of lowest magnitude. In the intermetallics, the valence band is of bonding character with positive COOP magnitudes; antibonding negative magnitude being found above E_F. This is opposed to the hydrogenated compounds where antibonding states, mainly Zr–Fe

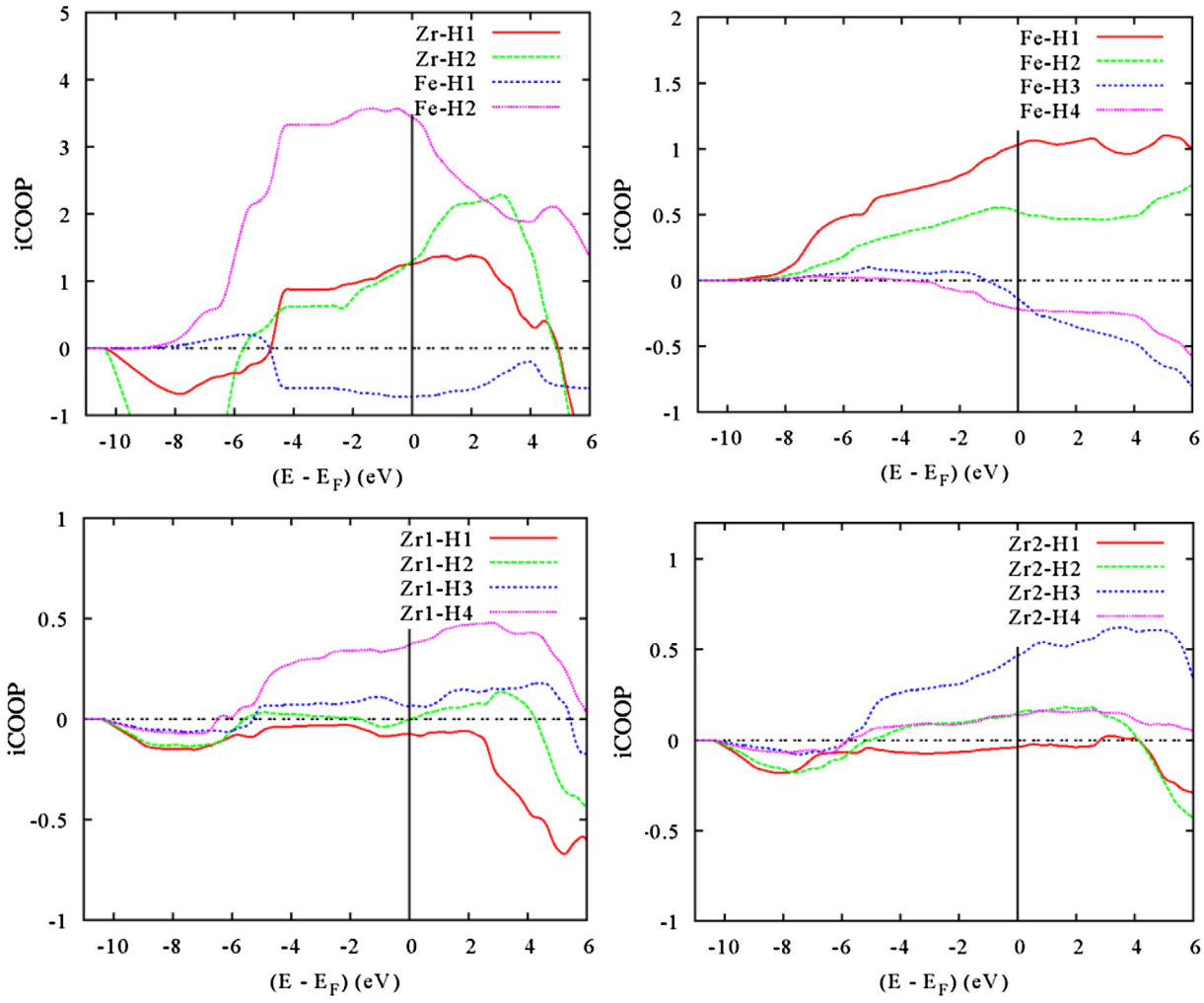

Fig. 5. Chemical bonding magnitudes of hydrogen with metal substructures in Zr_2FeH_5 (top left) and Zr_3FeH_7 (other three panels).

arise at the top of the valence band. Such a behavior is a signature of a weakening of Zr–Fe main bonding interaction due to the involved Zr and Fe valence states with the H bonding.

In order to compare bonding strengths, the integrated COOP, i.e. unit-less *i*COOP are displayed at Fig. 5 for the metal–H bonding in one panel for the 3:1:7 hydride. The larger the area below the *i*COOP curve, the larger the bonding is.

In Zr_2FeH_5 Zr as well as Fe are involved with H1 and H2 bonding. There are three main *i*COOP with decreasing intensities: Fe–H2, Zr–H2 and Zr–H1. They follow respectively from the presence of H2 in $[FeH_2]_4$ pyramidal motifs, H1 within $[Zr_4]$ tetrahedra and H2 surrounded by three more Zr than Fe in $[Zr_3Fe]$ tetrahedra. Nevertheless antibonding *i*COOP with negative intensities are observed especially for Zr–H2 because of the larger contribution of H2 states to the bonding with Fe in a competitive manner. Also Fe–H1 antibonding states arise from the competitive positive Zr–H1 bonding *i*COOP. Smaller contribution *i*COOP are found in the neighborhood of E_F with bonding Zr–H2 and antibonding Fe–H2.

For Zr_3FeH_7 *i*COOP Fe–H1 and Fe–H2 corresponding to the smallest Fe–H distances are most intense, followed by the Fe–H3 and Fe–H4 calculated at 2.04 and 2.05 Å lead to smaller Fe–H bonding intensities. The lower two panels presenting Zr–H bonding exhibit overall lower bonding versus Fe–H. *i*COOP intensities for Zr1–H and Zr2–H follow respective interatomic distances: $2.11 < d(\text{Zr1–H}) < 2.17$ Å whereas $2.04 < d(\text{Zr2–H}) < 2.18$ Å but remain close in intensities. As in 2:1:5 the Zr–H are antibonding in lower part of the valence band. Qualitatively the overall bonding in the 2:1:5 compound is larger than in the 3:1:7. This illustrates further the cohesive energies and the larger difference of bulk moduli identified above.

5. Conclusion

From the energy trends $E_{\text{coh.}}$ (ZrH_2) > $E_{\text{coh.}}$ (Zr_2FeH_5) > $E_{\text{coh.}}$ (Zr_3FeH_7) > $E_{\text{coh.}}$ (FeH) the emerging picture pertains to a destabilization of the binary hydride ZrH_2 by introducing Fe so that Zr_3FeH_7 is found less cohesive than Zr_2FeH_5. Consequently, larger Fe–H separation allows for magnetization to develop on Fe only in Zr_3FeH_7. Also the hydrogenation of the binary intermetallics is found to weaken the inter-metal bonding and favor the metal–hydrogen thus leading to more cohesive and harder hydrides as with respect to the pristine binaries. Charge analyses point to covalent like Fe versus ionic Zr and hydrogen charges ranging from covalent $H^{-0.27}$ to more ionic $H^{-0.5}$.

Acknowledgments

Part of this work was done in the framework of the CEDRE project between USEK and ICMCB-CNRS-University Bordeaux 1. Computational facilities provided by MCIA-University Bordeaux 1 are acknowledged.

References

[1] S.F. Matar, Prog. Solid State Chem. 38 (2010) 1–37 (a review).
[2] C.Z. Wu, P. Wang, X. Yao, C. Liu, D.M. Chen, G.Q. Lu, H.M. Cheng, J. Alloys Compd. 420 (2006) 278.
[3] M. Nakhl, M. Zakhour, Ch. Amine, H. El-Rassy, S.F. Matar, Adv. Mater. Res. 324 (2011) 119.
[4] S.F. Matar, Comput. Mater. Sci. 69 (2013) 424–427.
[5] J.J. Reilly, R.H. Wiswall Jr., Inorg. Chem. 7 (1968) 2254.
[6] W.R. Myers, L.-W. Wang, T.J. Richardson, M.D. Rubin, J. Appl. Phys. 91 (2002) 15.
[7] J. Zhang, D. Zhou, J. Liu, Trans. Nonferrous Met. Soc. China 19 (2009) 205.
[8] V.A. Yartys, H. Fjellvag, B.C. Hauback, A.B. Riabov, M.H. Sørby, K. Yvon, G. Renaudin, J. Alloys Compd. 278 (1998) 252.
[9] V.A. Yartys, H. Fjellvag, B.C. Hauback, A.B. Riabov, J. Alloys Compd. 274 (1998) 217.
[10] C. Guo, Zh. Du, Ch. Lia, B. Zhang, M. Tao, Calphad 32 (2008) 637.
[11] S.F. Matar, M. Nakhl, M. Zakhour, N. Ouaini, Lebanese Sci. J. 6 (2005) 107.
[12] B. Chabot, E. Parthé, Acta Crystallogr. B34 (1978) 3173.
[13] A. San-Martin, F.D. Manchester, Bull. Alloy Phase Diag. 11 (1990) 173.
[14] V.K. Fedotov, V.E. Antonov, T.E. Antonova, E.L. Bokhenkov, B. Dorner, G. Grosse, F.E. Wagner, J. Alloys Compd. 291 (1999) 1;
(a) R. Riane, A. Abdiche, L. Hamerelaine, M. Guemmou, N. Ouaini, S.F. Matar, Solid State Sci. 22 (2013) 77–81.
[15] P. Hohenberg, W. Kohn, Phys. Rev. B 136 (1964) 864.
[16] W. Kohn, L.J. Sham, Phys. Rev. A 140 (1965) 1133.
[17] G. Kresse, J. Furthmüller, Phys. Rev. B 54 (1996) 11169.
[18] G. Kresse, J. Joubert, Phys. Rev. B 59 (1999) 1758.
[19] P.E. Blöchl, Phys. Rev. B 50 (1994) 17953.
[20] J. Perdew, K. Burke, M. Ernzerhof, Phys. Rev. Lett. 77 (1996) 3865.
[21] D.M. Ceperley, B.J. Alder, Phys. Rev. Lett. 45 (1980) 566.
[22] W.H. Press, B.P. Flannery, S.A. Teukolsky, W.T. Vetterling, Numerical Recipes, Cambridge University Press, New York, 1986.
[23] M. Methfessel, A.T. Paxton, Phys. Rev. B 40 (1989) 3616.
[24] A.R. Williams, J. Kübler, C.D. Gelatt, Phys. Rev. B 19 (1979) 6094.
[25] V. Eyert, The Augmented Spherical Wave Method – a Comprehensive Treatment, Lecture Notes in Physics, Springer, Heidelberg, 2007.
[26] R. Hoffmann, Angew. Chem. Int. Ed. Engl. 26 (1987) 846.
[27] F. Birch, J. Geophys. Res. 83 (1978) 1257.
[28] S.F. Matar, G. Demazeau, M.H. Möller, R. Pöttgen, Chem. Phys. Lett. 508 (2011) 215.
[29] R. Bader, Chem. Rev. 91 (1991) 893.
[30] W. Tang, E. Sanville, G. Henkelman, J. Phys. Condens. Matter 21 (2009) 084204. http://theory.cm.utexas.edu/vtsttools/bader/.
[31] P. Mohn, Magnetism in the solid state – an introduction, Springer Series, in: M. Cardona, P. Fulde, K. von Klitzing, R. Merlin, H.J. Queisser, H. Störmer (Eds.), Solid-State Sciences, Springer, Heidelberg, 2003.
[32] J.F. Janak, Phys. Rev. B 16 (1977) 255.
[33] S.F. Matar, J. Solid State Chem. 200 (2013) 209.